

# Broken intrinsic symmetry induced magnon-magnon coupling in synthetic ferrimagnets

Mohammad Tomal Hossain,<sup>1</sup> Hang Chen,<sup>1</sup> Subhash Bhatt,<sup>1</sup> Mojtaba Taghipour Kaffash,<sup>1</sup> John Q. Xiao,<sup>1</sup> Joseph Sklenar,<sup>2</sup> and M. Benjamin Jungfleisch<sup>1, \*</sup>

<sup>1</sup>*Department of Physics and Astronomy, University of Delaware, Newark, Delaware 19716, USA*

<sup>2</sup>*Department of Physics and Astronomy, Wayne State University, Detroit, MI 48202, USA*

(Dated: October 10, 2024)

Synthetic antiferromagnets offer rich magnon energy spectra in which optical and acoustic magnon branches can hybridize. Here, we demonstrate a broken intrinsic symmetry induced coupling of acoustic and optical magnons in a synthetic ferrimagnet consisting of two dissimilar antiferromagnetically interacting ferromagnetic metals. Two distinct magnon modes hybridize at degeneracy points, as indicated by an avoided level-crossing. The avoided level-crossing gap depends on the interlayer exchange interaction between the magnetic layers, which can be controlled by adjusting the non-magnetic interlayer thickness. An exceptionally large avoided level crossing gap of 6 GHz is revealed, exceeding the coupling strength that is typically found in other magnonic hybrid systems based on a coupling of magnons with photons or magnons and phonons.

## I. INTRODUCTION

Magnons are the quanta of spin waves representing the fundamental excitation of the magnetic order in a magnetic system. Magnons play a crucial role in our understanding of magnetism. They have been the subject of extensive study for their properties and applications in various technologies, particularly in the development of novel magnonic devices [1–7]. Antiferromagnetic magnons are investigated for their potential use in ultrafast applications including next-generation memory devices and information processing [8–12], terahertz spectroscopy and imaging [13–17], and quantum computing [18]. Giant magnetoresistance (GMR) was discovered in 1988 in antiferromagnetically coupled layered ferromagnetic (FM) structures [19, 20]. This marks one of the initial applications of synthetic antiferromagnetic (sAF) heterostructures comprising two ferromagnetic metal layers coupled antiferromagnetically. This idea expanded to various other devices such as magnetic tunnel junctions and spin-torque nano-oscillators [21–23]. sAFs offer several engineering advantages compared to bulk antiferromagnets. Unlike bulk antiferromagnetic materials, sAFs can be tailored with specific layer thicknesses and compositions, which allows for the optimization of magnetic properties such as exchange bias, coercivity, and anisotropy. These engineering opportunities make sAFs ideal model systems for studying antiferromagnetic magnons.

Coupling between magnon modes in sAFs can lead to the exchange of energy and momentum between different magnon modes. By controlling the coupling strength, the propagation and transmission of spin waves can be manipulated. This can improve performance in magnonic devices such as magnon transistor [24], and magnon logic

elements [25]. The most dominant mechanisms responsible for magnon-magnon coupling are the exchange interaction (short range) [26] and the dipolar interaction (long range) [27]. In sAFs comprising two sublattices with antiferromagnetic exchange interaction, two distinct normal modes can emerge based on the relative motion of the spins precessing in the sublattices; in-phase motion (acoustic mode) or out-of-phase motion (optical mode). Generally, these modes are protected by symmetry, preventing them from coupling [28]. Strategies to facilitate magnon-magnon coupling in sAFs have been studied recently [27, 29–33].

Furthermore, a recent theoretical work suggested the possibility of magnon-magnon coupling for an in-plane geometry in an intrinsic symmetry-breaking mechanism using a synthetic ferrimagnetic structure [34]. Ferrimagnets are partially compensated magnetic structures in which the sublattices with unequal magnetic moments are arranged in opposite directions, which results in non-zero spontaneous magnetization. In a synthetic structure, this can be achieved in different ways, such as by using FM layers with different saturation magnetization,  $M_s$ , by using different thicknesses of the FM layers,  $d$ , by using an unequal number of layers, or any combination of them, all connected by negative RKKY [35] interaction between layers [36–42]. Synthetic ferrimagnets can facilitate intrinsic symmetry breaking in the presence of RKKY and biquadratic interactions, which leads to the coupling of acoustic and optical modes [34].

Here, we report the experimental observation of such magnon-magnon coupling induced by broken intrinsic symmetry in synthetic ferrimagnetic structures. We use two antiferromagnetically interacting magnetic layers of similar thickness,  $d$ , but different saturation magnetization,  $M_s$  (CoFe and NiFe) separated by a thin spacer layer (Ru). Magnetometry using vibrating sample magnetometry (VSM) reveals the exchange interaction between the ferromagnetic layers. Using two complementary techniques, spin-torque ferromagnetic resonance (STFMR)

---

\* mbj@udel.edu

and Brillouin light scattering (BLS), we show that the asymmetry introduced by broken intrinsic symmetry facilitates the coupling between the acoustic and optical magnon modes. Furthermore, our studies reveal that the coupling strength between the modes can be tuned by controlling the exchange interaction between the ferromagnetic layers. Our experimental results are systematically compared with micromagnetic simulations using Mumax3 [43]. This study aims to leverage the magnon-magnon interaction within an in-plane geometry to develop innovative magnonic device applications.

## II. SAMPLE FABRICATION AND EXPERIMENTAL DETAILS

Figure 1(a) illustrates a schematic of the synthetic ferrimagnetic sample stack. The samples comprise a trilayer of  $\text{Co}_{90}\text{Fe}_{10}$  (10 nm)/Ru( $d$  nm)/ $\text{Ni}_{80}\text{Fe}_{20}$  (10 nm) with varying thickness  $d$  of the non-magnetic spacer layer Ru. The structure was grown on thermally oxidized Si substrates at room temperature under an Ar pressure of  $4.5 \times 10^{-3}$  Torr in a magnetron sputtering system with a base pressure of  $1.4 \times 10^{-7}$  Torr. The Ru spacer layer was grown in a wedge shape, allowing for a continuous

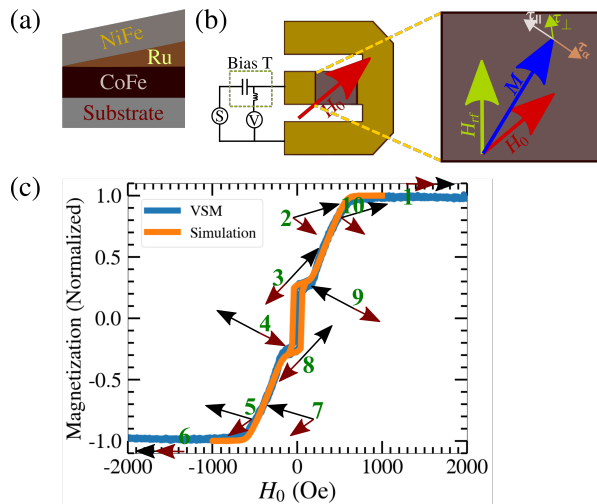


Figure 1. (a) Schematic illustration of the synthetic ferrimagnet comprising of a  $\text{CoFe}/\text{Ru}/\text{NiFe}$  heterostructure. The thickness of Ru is varied from 0 nm to 1 nm to tune the coupling strength between  $\text{CoFe}$  and  $\text{NiFe}$ . (b) Illustration of the spin-torque ferromagnetic resonance (STFMR) setup, including an inset that shows the relevant torques on the magnetization  $M$ :  $\tau_{\parallel}$  - anti-damping-like torque,  $\tau_{\alpha}$  - damping-like torque,  $\tau_{\perp}$  - field-like torque. The biasing field  $H_0$  is applied at an angle of 45 degrees with respect to the microwave field  $H_{\text{rf}}$ . (c) Magnetometry measurement using vibrating sample magnetometry (VSM) for a 0.8 nm Ru thickness and the corresponding simulation results obtained using Mumax3. The simulation agrees reasonably well with the experiment. The arrows indicated the relative alignment of the two exchange-coupled ferromagnetic layers.

thickness variation from  $d = 0$  to 1 nm at an wedge angle of about  $1 \mu\text{deg}$ , by off-center deposition to tune the interlayer exchange interaction. All samples were capped with a 5 nm  $\text{SiO}_2$  layer to protect the sample from oxidation. The sample was then cut into 11 rectangular samples where the thickness of the spacer layer can be considered approximately constant over the width of each sample. The anisotropic easy axes in the FM layers were introduced along the long sides of the samples. VSM measurements were performed to characterize the static magnetic properties of the individual pieces of the sample. Figure 1(c) shows a typical VSM measurement of a synthetic ferrimagnet with negative RKKY interaction between the ferromagnetic layers, which we discuss below.

To investigate the spin dynamics in the ferrimagnet, we use a combined STFMR and BLS spectroscopy approach. The STFMR signal is the spin rectification of the magnetoresistance in the device [44], which provides high sensitivity measurements. In STFMR measurements a spin-polarized current in addition to an rf magnetic field exerts a torque on the magnetization, causing it to precess when the resonance condition is realized. This precession induces a time-varying magnetization, consequently giving rise to an AC resistance as a result of the anisotropic magnetoresistance or spin Hall magnetoresistance [45, 46]. This, combined with the AC current passed through the sample at the same frequency, generates a rectified DC voltage, which is measured using a lock-in amplifier [47]. For STFMR measurements, the sputtered thin films were etched to produce STFMR devices following the following steps: first, a negative-tone photoresist was used to cover  $80 \mu\text{m} \times 130 \mu\text{m}$  rectangular sections of the film, followed by etching using Ar ion milling of the surrounding film. The shorted coplanar waveguides were then patterned on top of the rectangular sections using optical lithography and positive photoresist. Finally, 5 nm of Ti and 20 nm of Au were e-beam evaporated and lifted off to create the waveguides on the devices as shown in Fig. 1(b).

A bias tee was used to simultaneously apply a microwave current and measure the rectified DC voltage using a lock-in amplifier [48]. A microwave frequency signal of +21 dBm power was supplied by an Agilent E8257D signal generator modulated with a frequency of 666.7 Hz. The external magnetic field  $H_0$  was applied in the sample plane at an angle of  $45^\circ$  with respect to the device to achieve maximum signal strength [47, 49]. The microwave frequency was swept from 1 to 18 GHz in 86 steps, with the external field being varied from +2000 to 0 Oe for each frequency step.

As a spin rectification measurement, STFMR probes the excited magnons indirectly. An alternative approach is thermal BLS, which directly measures the magnon population in the magnetic material at a given temperature. We used microfocused thermal BLS measurements at room temperature in a backscattering geometry using a 532 nm continuous wave single-mode laser and a high-numerical aperture  $100\times$  objective lens ( $\text{NA} = 0.75$ ).

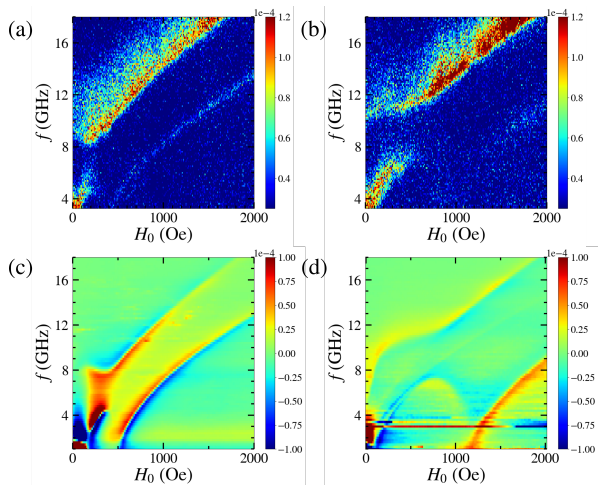


Figure 2. Experimentally observed magnon spectra. Thermal Brillouin light scattering spectra for (a) a Ru thickness of 0.8 nm and (b) for a Ru thickness of 0.4 nm. (c) and (d) show the corresponding STFM spectra, respectively.

The inelastically scattered light was passed through a high-contrast multi-pass tandem Fabry P erot interferometer with a contrast of at least  $10^{15}$ . The external field was swept from +2000 Oe to 0 Oe. For each field value, the anti-Stokes BLS spectrum was recorded. The acquisition time for the spectrum at each field was 3 min.

### III. RESULTS AND DISCUSSION

As is shown in Fig. 1(c), magnetometry measurements show a typical hysteresis loop of a synthetic antiferromagnet. Magnetometry measurements show secondary loops in the hysteresis for Ru thicknesses above 0.2 nm [see Fig. S2 in the supplementary materials (SM)]. From 0.2 – 0.5 nm, two secondary loops appear near the *knee* (the field at which the magnetization changes from saturated to unsaturated), while above 0.5 nm, a loop forms at the center [Fig. 1(c)]. The ‘*knee* loops’ suggest the presence of biquadratic exchange interaction between FM films for Ru thicknesses of 0.2–0.5 nm [50] (see SM). The magnetometry results can be explained by carefully analyzing the expression of the volume energy density of the structure [51]:

$$\mathcal{E} = -\vec{M} \cdot \vec{H}_0 + J_q \hat{n}_1 \cdot \hat{n}_2 + J_{bq} (\hat{n}_1 \cdot \hat{n}_2)^2. \quad (1)$$

Here,  $\vec{M}$  is the magnetization,  $H_0$  is the external magnetic field,  $\hat{n}_i$  and  $M_{S_i}$  are the magnetization unit vectors and saturation magnetization of the  $i$ -th layer ( $i = 1, 2$ ), respectively.  $J_q$  and  $J_{bq}$  are the phenomenological energy densities for quadratic and biquadratic exchange interaction. RKKY interaction is negative (i.e., favoring antiferromagnetic alignment of the magnetic layers) when  $J_q$  is positive. At a large field, the magnetostatic energy is

large enough to saturate both layers in the direction of the field [labeled ‘1’ in Fig. 1(c)]. As the field is reduced, a field is reached [labeled ‘2’ in Fig. 1(c)] where the exchange energy becomes significant and attempts to align the FM layers antiferromagnetically. As a result, the two layers reach an equilibrium at a tilted angle with respect to each other away from the saturated state, reducing the net magnetization. The field at which the magnetization starts to reduce (i.e., the *knee* field in the hysteresis loop) can be calculated using a macrospin model as in Eq. (1) (see SM for the derivation):

$$H_{0,ff} = (J_q + 2J_{bq}) \left( \frac{1}{M_{S1}} + \frac{1}{M_{S2}} \right), \quad (2a)$$

where  $H_{0,ff}$  is the magnitude of the magnetic field over which the FM layers align in a forced ferromagnetic state [point ‘1’ in Fig. 1(c)].

If the biquadratic exchange interaction is negligible, magnetization changes linearly with the external field in the unsaturated region [between point ‘2’ and ‘3’ in Fig. 1(c)] (see SM for derivation). However, strong biquadratic interaction causes a non-linear relation, creating secondary loops near the knee field in the hysteresis (see SM). As the external field decreases further, the quadratic exchange energy dominates, forming a plateau [point ‘3’ in Fig. 1(c)] with antiparallel layer alignment (see SM). The finite magnetization at this plateau results from different saturation magnetizations between the ferromagnetic layers [52], creating the central loop in the magnetometry data, as seen in Fig. 1(c). The field at which the layers antiferromagnetically align is given by Eq. (2b):

$$H_{0,afm} = (J_q - 2J_{bq}) \left( \frac{1}{M_{S2}} - \frac{1}{M_{S1}} \right), \quad (2b)$$

with  $M_{S1} > M_{S2}$ . Equation (2b) explains the absence of a central secondary loop in magnetometry when Ru thickness is less than 0.6 nm, given  $J_q < 2J_{bq}$  makes  $H_{0,afm}$  negative, preventing a fully antiferromagnetic state. Eqs. (2a) and (2b) provide a means to extract  $J_q$  and  $J_{bq}$  from magnetometry measurements when  $J_q > 2J_{bq}$ , allowing a fully antiferromagnetic state:

$$J_q = \left( \frac{H_{0,ff}}{M_{S1} + M_{S2}} + \frac{H_{0,afm}}{M_{S1} - M_{S2}} \right) \frac{M_{S1}M_{S2}}{2}, \quad (3a)$$

$$J_{bq} = \left( \frac{H_{0,ff}}{M_{S1} + M_{S2}} - \frac{H_{0,afm}}{M_{S1} - M_{S2}} \right) \frac{M_{S1}M_{S2}}{4}. \quad (3b)$$

The relationship between the saturation magnetizations of the ferromagnetic layers can be established using the normalized magnetization of the forced ferromagnetic ( $M_{ff}$ ) and fully antiferromagnetic ( $M_{afm}$ ) states [magnetization at point ‘2’ to point ‘3’ in Fig. 1(c), respectively].

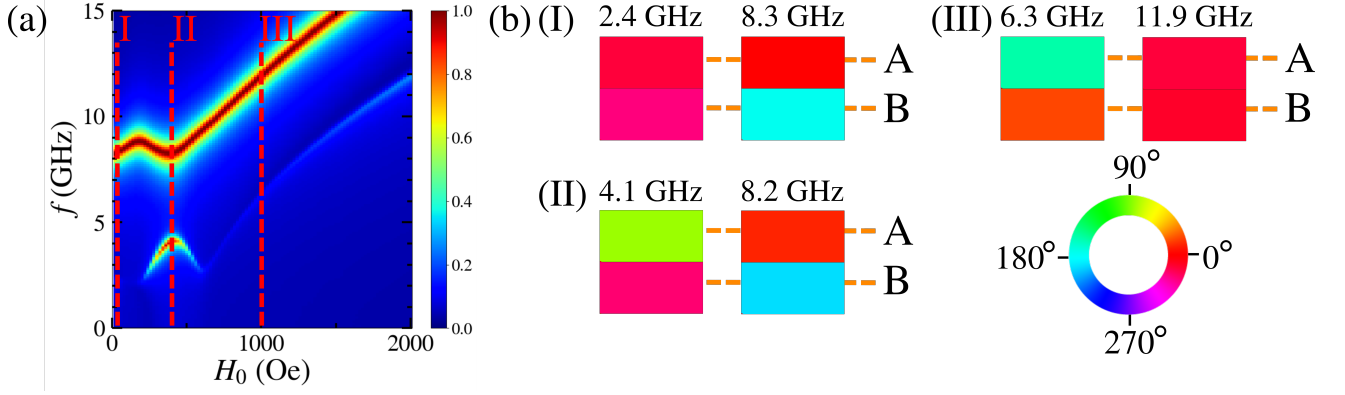


Figure 3. Micromagnetic simulation results obtained by Mumax3. (a) Simulated spectrum for a Ru thickness of 0.8 nm. (b) Corresponding spatially-resolved simulations reveal the phase profiles of the magnon modes in the top (A) and bottom (B) layer extracted from the FFTs of the spatial simulation at (I) 40 Oe, (II) 400 Oe, and (III) 1000 Oe. Top panel (A) is the NiFe layer, bottom panel (B) is the CoFe layer. The inset shows a color wheel indicating the phase.

The ratio of the saturation magnetizations can be expressed as follows:

$$\frac{M_{S2}}{M_{S1}} = \frac{M_{ff} - M_{afm}}{M_{ff} + M_{afm}}. \quad (4)$$

For a Ru thickness of 0.8 nm, we find  $M_{ff} = 1.0$  and  $M_{afm} = 0.29$ . The saturation magnetization used in this work for NiFe was taken from literature to be 10.1 kOe [53], which allows us to calculate the saturation magnetization of CoFe to be 18.5 kOe using Eq. (4). From magnetometry measurements in Fig. 1(c) we found  $H_{0,ff}$  and  $H_{0,afm}$  to be 590 Oe and 155 Oe, respectively. This provides values for  $J_q$  and  $J_{bq}$  to be 2.95 kJ/m<sup>3</sup> and 0.74 kJ/m<sup>3</sup>, respectively, using Eqs. (3a) and (3b).

To gain a better understanding of the experimental results, we performed micromagnetic modeling using the graphics processor unit (GPU)-accelerated program Mumax3 [43, 54]. Our structure was modeled as  $128 \times 64 \times 3$  cells with an individual cell size of 4.0 nm  $\times$  4.0 nm  $\times$  4.0 nm, with the middle layer representing the spacer. Each layer was defined into a region to set material parameters separately. The values for the exchange stiffness of CoFe and NiFe used in the simulation were  $3.0 \times 10^{-11}$  J/m and  $1.3 \times 10^{-11}$  J/m, respectively [55]. This corresponds to exchange lengths for NiFe and CoFe of 5.29 nm and 4.32 nm, respectively [55]. Crystalline anisotropy was added for the CoFe layer with a crystalline anisotropy constant of  $K = -30 \times 10^3$  J/m<sup>3</sup> along the (1 0 0) direction [55]. The following Gilbert damping constants were used for CoFe and NiFe, respectively:  $\alpha_{CoFe} = 0.005$  [56] and  $\alpha_{NiFe} = 0.0095$  [57]. We define quadratic and biquadratic interactions between magnetic layers using a custom exchange field and energy density, leading to the exchange energy in Eq. (1) (third and fourth terms on the right) that satisfies the form:

$$\mathcal{E}_{\text{exch}} = -\frac{1}{2} \vec{M} \cdot \vec{H}_{\text{exch}}. \quad (5)$$

We can split the exchange field into quadratic and biquadratic terms as  $\vec{H}_{\text{exch}} = \vec{H}_{\text{quad}} + \vec{H}_{\text{biquad}}$ , which leads to the expressions for quadratic and biquadratic exchange fields given by:

$$\vec{H}_{\text{quad}} = -\frac{2J_q}{M_{S1}M_{S2}} \vec{M}, \quad (6a)$$

$$\vec{H}_{\text{biquad}} = -\frac{2J_{bq}}{(M_{S1}M_{S2})^2} (\vec{M} \cdot \vec{M}) \vec{M}. \quad (6b)$$

Here,  $\vec{M}$  is the swapped magnetization defined as  $\vec{M}(x, y, z, t) = \vec{M}(x, y, -z, t)$ .

We first performed magnetostatic simulations to generate the hysteresis loop. The simulation started with a static magnetic field of +2000 Oe along the long axis, swept down to -2000 Oe in steps of 20 Oe, and ramped up back to +2000 Oe to complete the hysteresis loop. The built-in relaxation function in Mumax3 was used to find the equilibrium state of the system. The simulated hysteresis loops agree well with the results obtained by the VSM measurements, as shown in Fig. 1(c).

In the following, the dynamics measurements are discussed and compared to micromagnetic simulations. The spin dynamics was measured for 11 samples with increasing thickness of Ru varying from 0 nm to 1 nm by STFMR and thermal BLS techniques. Figure 2 compares the thermal BLS and STFMR spectra for samples with Ru thicknesses of 0.8 nm and 0.4 nm, both showing antiferromagnetic interaction in the magnetometry measurements (see Fig. S2). We notice two magnon modes in the spectra of all of our samples with negative RKKY interaction (as found in magnetometry measurements; see also SM). These two modes correspond to the optical and acoustic modes. Typically, these two modes are protected by symmetry, which means that they cross at the degeneracy point. As is evident from Fig. 2, that is not what we observe in the experiments: a clear avoided-level

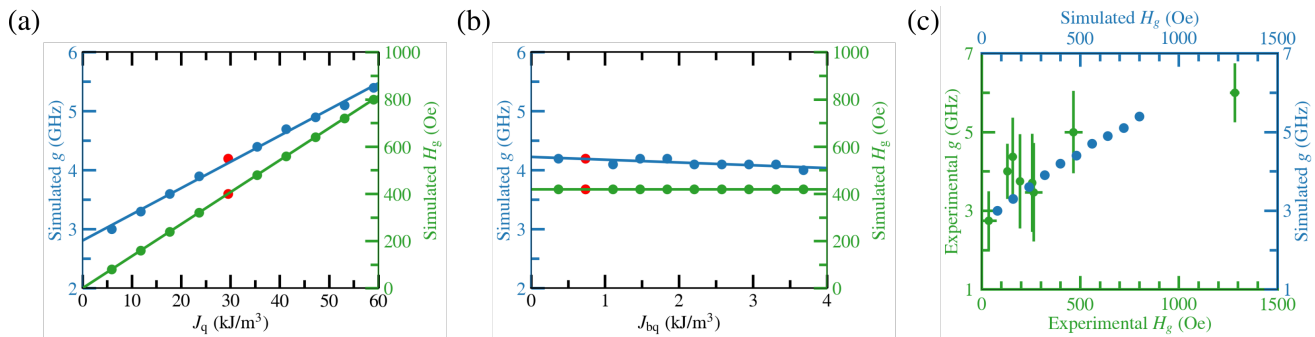


Figure 4. (a) Simulated coupling gap  $g$  (blue) and simulated degeneracy field  $H_g$  (green) vs. quadratic interaction constant  $J_q$  at a fixed biquadratic interaction constant  $J_{bq} = 0.74 \text{ kJ/m}^3$ . The degeneracy field  $H_g$  was determined as the field where the high- and low-frequency modes have the smallest separation in frequency ( $g$ ). Solid lines represent linear fits with respect to  $J_q$ . (b) Simulated coupling gap  $g$  (blue) and simulated degeneracy field  $H_g$  (green) vs. biquadratic interaction constant  $J_{bq}$  at a fixed quadratic interaction constant  $J_q = 29.5 \text{ kJ/m}^3$ . Solid lines represent linear fits with respect to  $J_{bq}$ . Red points indicate the simulation conditions resembling the experimental conditions for a Ru thickness of 0.8 nm. (c) Experimentally observed gap vs. degeneracy field (green) and simulated gap vs. degeneracy field (blue). The experimental data points are extracted from the BLS measurements. STFMR measurements show a similar linear trend for gap vs. degeneracy field.

crossing is found at the degeneracy points, indicating a strong coupling between optical and acoustic modes. We observe the largest gap of 6 GHz for the sample with 0.4 nm of Ru thickness. The BLS spectrum qualitatively agrees with the STFMR spectrum for each sample. When comparing the BLS and STFMR measurements, we observe that the BLS intensity is less prominent for a particular mode, which corresponds to the optical mode, as discussed below. We speculate that this could be due to either the lower magnon population in the optical branch in the thermal BLS experiments or due to a lower BLS detection sensitivity to optical modes.

Micromagnetic simulations using Mumax3 reveal mode phase relations between the ferromagnetic layers in the dynamic spectra. Figure 3 simulates a synthetic ferrimagnetic structure with 0.8 nm Ru thickness, corresponding to experimental BLS and STFMR measurements in Figs. 2(a) and (c). The spectrum shows two hybridized magnon modes. Spatially-resolved micromagnetic modeling shows in-phase or out-of-phase modes away from the energy degeneracy point, corresponding to acoustic or optical modes [Fig. 3(b)]. At 40 Oe [marked ‘I’ in Fig. 3(a)], two modes are observed: a low-frequency mode at 2.4 GHz and a high-frequency mode at 8.3 GHz. The corresponding spatially-resolved simulations reveal the phase profile of the top and the bottom layer, see Fig. 3(b). As is evident from the figure, the top and the bottom layers are in-phase at 2.4 GHz (acoustic mode), while they are out-of-phase at 8.3 GHz (optical mode). The two modes are well-separated in frequency from one another; hence, they are uncoupled. At 1000 Oe [marked ‘III’ in Fig. 3(a)], the high-frequency mode is the acoustic mode, while the low-frequency mode is the optical mode, as can be seen from the spatially-resolved simulations shown in Fig. 3(b). Between 40 and 1000 Oe (field region between vertical dashed line ‘I’ and ‘III’), the low- and high-frequency modes exchange their character from

acoustic to optical. As can be seen in Fig. 3(a), the two modes repel each other near the degeneracy point marked ‘II’, leading to an avoided level crossing and a gap in the spectrum (see SM for more details on the phase analysis). The corresponding spatially-resolved simulations reveal a ‘mixed’ phase relationship, Fig. 3(b). The modes are no longer purely acoustic or optical in nature. The opening of a gap at the degeneracy field is the signature of a strong coupling between the acoustic and optical modes. The results obtained by simulations (Fig. 3) support the experimental results (Fig. 2), corroborating a strong coupling between the modes. We argue that this strong coupling between acoustic and optical magnons is facilitated by exchange interaction induced by broken intrinsic symmetry in the studied synthetic ferrimagnet [58].

The micromagnetic simulations also allow us to examine the dependence of gap size ( $g$ ) and field ( $H_g$ ) on quadratic and biquadratic interaction: Figure 4(a) shows that  $g$  and  $H_g$  linearly increase with the quadratic interaction constant  $J_q$ . The corresponding simulated spectra are presented in the SM. Furthermore, we used the simulations to extract the dependence of  $g$  and  $H_g$  on the biquadratic interaction  $J_{bq}$ : Figure 4(b) demonstrates a minimal dependence of  $g$  and  $H_g$  on  $J_{bq}$ . The simulated  $J_b$  and  $J_{bq}$  corresponding to the experimental conditions found for a Ru thickness of 0.8 nm are shown as red data points in Figs. 4(a) and (b) for reference. In addition, we plot the experimentally obtained and simulated dependence between  $g$  and  $H_g$  in Fig. 4(c). The overall trend matches remarkably well (please note that each experimental data point in Fig. 4(c) has different values for  $J_b$  and  $J_{bq}$ , whereas different values of  $J_b$  were used for the simulated data points while  $J_{bq}$  was kept fixed). The micromagnetic simulations are particularly useful to determine  $J_q$  and  $J_{bq}$  even when  $J_q < 2J_{bq}$ , in which case Eq. (3) is inapplicable due to incomplete antiferromagnetic alignment and undefined value of  $H_{afm}$ .

We discuss this approach in the following: If full antiferromagnetic alignment is experimentally achieved for a particular Ru thickness,  $J_q$  and  $J_{bq}$  can be obtained from the magnetometry results [Fig. 1 and Eqs. (3a) and (3b)]. At the same time,  $H_g$  can be determined from spin dynamics measurements such as STFMR or BLS. Since  $H_g$  is linearly proportional to  $J_q$ , we can calculate the proportionality constant using linear regression for a given sample with a particular Ru thickness. This constant then allows us to determine  $J_q$  for any Ru thickness, even without full antiferromagnetic alignment. Finally,  $J_{bq}$  can be determined with the knowledge of  $J_q$  and Eq. (2a). This method is a powerful tool for determining the biquadratic exchange interaction of any system.

#### IV. SUMMARY

In summary, we demonstrated strong coupling between acoustic and optical modes in an in-plane geometry through broken intrinsic symmetry in a synthetic ferrimagnetic structure comprising of CoFe(10 nm)/Ru( $x$  nm)/NiFe(10 nm). Micromagnetic

simulations using Mumax3 reveal that both the gap field and the size of the gap depend on the quadratic interaction  $J_q$ , while they are almost independent of the biquadratic interaction,  $J_{bq}$ . Furthermore, the simulations allow us to unambiguously distinguish between the optical and acoustic modes observed in the experiment, and the phase analysis shows that the modes are indeed hybridized at the degeneracy field. Our study introduces intrinsic symmetry-breaking as a mechanism to tune magnon-magnon interaction in an in-plane geometry, providing intriguing opportunities for engineered magnonic hybrid systems.

#### ACKNOWLEDGEMENTS

This research was supported by NSF through the University of Delaware Materials Research Science and Engineering Center, DMR-2011824. The authors acknowledge the use of facilities and instrumentation supported by NSF through the University of Delaware Materials Research Science and Engineering Center, DMR-2011824.”

The data supporting this study’s findings are available upon reasonable request.

- 
- [1] J. Chen, H. Yu, and G. Gubbiotti, *Journal of Physics D: Applied Physics* **55**, 123001 (2021).
- [2] A. Haldar, D. Kumar, and A. O. Adeyeye, *Nature Nanotechnology* **11**, 437 (2016).
- [3] S. Urazhdin, V. E. Demidov, H. Ulrichs, T. Kendziorczyk, T. Kuhn, J. Leuthold, G. Wilde, and S. O. Demokritov, *Nature Nanotechnology* **9**, 509 (2014).
- [4] A. Khitun, M. Bao, and K. L. Wang, *Journal of Physics D: Applied Physics* **43**, 264005 (2010).
- [5] A. Mahmoud, F. Ciubotaru, F. Vanderveken, A. V. Chumak, S. Hamdioui, C. Adelmann, and S. Cotozana, *Journal of Applied Physics* **128**, 161101 (2020).
- [6] A. V. Chumak, P. Kabos, M. Wu, C. Abert, C. Adelmann, A. O. Adeyeye, J. Åkerman, F. G. Aliev, A. Anane, A. Awad, C. H. Back, A. Barman, G. E. W. Bauer, M. Becherer, E. N. Beginin, V. A. S. V. Bitencourt, Y. M. Blanter, P. Bortolotti, I. Boventer, D. A. Bozhko, S. A. Bunyaev, J. J. Carmiggelt, R. R. Cheenikundil, F. Ciubotaru, S. Cotozana, G. Csaba, O. V. Dobrovolskiy, C. Dubs, M. Elyasi, K. G. Fripp, H. Fulara, I. A. Golovchanskiy, C. Gonzalez-Ballesteros, P. Graczyk, D. Grundler, P. Gruszecki, G. Gubbiotti, K. Guslienko, A. Haldar, S. Hamdioui, R. Hertel, B. Hillebrands, T. Hioki, A. Houshang, C.-M. Hu, H. Huebl, M. Huth, E. Iacocca, M. B. Jungfleisch, G. N. Kakazei, A. Khitun, R. Khymyn, T. Kikkawa, M. Kläui, O. Klein, J. W. Klos, S. Knauer, S. Koraltan, M. Kostylev, M. Krawczyk, I. N. Krivorotov, V. V. Kruglyak, D. Lachance-Quirion, S. Ladak, R. Lebrun, Y. Li, M. Lindner, R. Macêdo, S. Mayr, G. A. Melkov, S. Mieszczak, Y. Nakamura, H. T. Nembach, A. A. Nikitin, S. A. Nikitov, V. Novosad, J. A. Otálora, Y. Otani, A. Papp, B. Pigeau, P. Pirro, W. Porod, F. Porrati, H. Qin, B. Rana, T. Reimann, F. Riante, O. Romero-Isart, A. Ross, A. V. Sadovnikov, A. R. Safin, E. Saitoh, G. Schmidt, H. Schultheiss, K. Schultheiss, A. A. Serga, S. Sharma, J. M. Shaw, D. Suess, O. Surzhenko, K. Szulc, T. Taniguchi, M. Urbánek, K. Usami, A. B. Ustinov, T. van der Sar, S. van Dijken, V. I. Vasyuchka, R. Verba, S. V. Kusminskiy, Q. Wang, M. Weides, M. Weiler, S. Wintz, S. P. Wolfski, and X. Zhang, *IEEE Transactions on Magnetics* **58**, 1 (2022), conference Name: IEEE Transactions on Magnetics.
- [7] Q. Wang, G. Csaba, R. Verba, A. V. Chumak, and P. Pirro, *Physical Review Applied* **21**, 040503 (2024), publisher: American Physical Society.
- [8] D. Xiong, Y. Jiang, K. Shi, A. Du, Y. Yao, Z. Guo, D. Zhu, K. Cao, S. Peng, W. Cai, D. Zhu, and W. Zhao, *Fundamental Research* **2**, 522 (2022).
- [9] T. Kosub, M. Kopte, R. Hühne, P. Appel, B. Shields, P. Maletinsky, R. Hübner, M. O. Liedke, J. Fassbender, O. G. Schmidt, and D. Makarov, *Nature Communications* **8**, 13985 (2017).
- [10] K. Olejník, V. Schuler, X. Marti, V. Novák, Z. Kašpar, P. Wadley, R. P. Champion, K. W. Edmonds, B. L. Gallagher, J. Garces, M. Baumgartner, P. Gambardella, and T. Jungwirth, *Nature Communications* **8**, 15434 (2017).
- [11] K. Olejník, T. Seifert, Z. Kašpar, V. Novák, P. Wadley, R. P. Champion, M. Baumgartner, P. Gambardella, P. Němec, J. Wunderlich, J. Sinova, P. Kužel, M. Müller, T. Kampfrath, and T. Jungwirth, *Science Advances* **4**, eaar3566 (2018).
- [12] M. B. Jungfleisch, J. Sklenar, J. Ding, J. Park, J. E. Pearson, V. Novosad, P. Schiffer, and A. Hoffmann, *Physical Review Applied* **8**, 064026 (2017), publisher: American

- Physical Society.
- [13] H. Lee, T. S. Jung, H. J. Shin, S. H. Oh, K. I. Sim, T. Ha, Y. J. Choi, and J. H. Kim, *Applied Physics Letters* **119**, 192903 (2021).
- [14] E. Rongione, O. Gueckstock, M. Mattern, O. Gomonay, H. Meer, C. Schmitt, R. Ramos, T. Kikkawa, M. Mićica, E. Saitoh, J. Sinova, H. Jaffrès, J. Mangeney, S. T. B. Goennenwein, S. Geprägs, T. Kampfrath, M. Kläui, M. Bargheer, T. S. Seifert, S. Dhillon, and R. Lebrun, *Nature Communications* **14**, 1818 (2023), number: 1 Publisher: Nature Publishing Group.
- [15] E. Mashkovich, K. Grishunin, R. Mikhaylovskiy, A. Zvezdin, R. Pisarev, M. Strugatsky, P. Christianen, T. Rasing, and A. Kimel, *Physical Review Letters* **123**, 157202 (2019).
- [16] P. Bowlan, S. A. Trugman, D. A. Yarotski, A. J. Taylor, and R. P. Prasankumar, *Journal of Physics D: Applied Physics* **51**, 194003 (2018).
- [17] W. Wu, C. Yaw Ameyaw, M. F. Doty, and M. B. Jungfleisch, *Journal of Applied Physics* **130**, 091101 (2021).
- [18] F. Meier, J. Levy, and D. Loss, *Physical Review B* **68**, 134417 (2003).
- [19] M. N. Baibich, J. M. Broto, A. Fert, F. N. Van Dau, F. Petroff, P. Etienne, G. Creuzet, A. Friederich, and J. Chazelas, *Physical Review Letters* **61**, 2472 (1988).
- [20] G. Binasch, P. Grünberg, F. Saurenbach, and W. Zinn, *Physical Review B* **39**, 4828 (1989).
- [21] J. Grollier, D. Querlioz, and M. D. Stiles, *Proceedings of the IEEE* **104**, 2024 (2016).
- [22] S. I. Kiselev, J. C. Sankey, I. N. Krivorotov, N. C. Emley, R. J. Schoelkopf, R. A. Buhrman, and D. C. Ralph, *Nature* **425**, 380 (2003).
- [23] K. Luo, Y. Guo, W. Li, B. Zhang, B. Wang, and J. Cao, *Journal of Applied Physics* **133**, 153902 (2023).
- [24] S.-J. Gong, C. Gong, Y.-Y. Sun, W.-Y. Tong, C.-G. Duan, J.-H. Chu, and X. Zhang, *Proceedings of the National Academy of Sciences* **115**, 8511 (2018).
- [25] A. V. Chumak, *Arxiv* **1901.08934** (2019).
- [26] D. MacNeill, J. T. Hou, D. R. Klein, P. Zhang, P. Jarillo-Herrero, and L. Liu, *Physical Review Letters* **123**, 047204 (2019), publisher: American Physical Society.
- [27] Y. Shiota, T. Taniguchi, M. Ishibashi, T. Moriyama, and T. Ono, *Physical Review Letters* **125**, 017203 (2020), publisher: American Physical Society.
- [28] J. P. Patches, M. Drouhin, J. W. Liao, Z. Soban, D. Petit, J. Haigh, P. Roy, J. Wunderlich, R. P. Cowburn, and C. Ciccarelli, *Physical Review B* **105**, 104436 (2022).
- [29] A. Sud, C. W. Zollitsch, A. Kamimaki, T. Dion, S. Khan, S. Iihama, S. Mizukami, and H. Kurebayashi, *Physical Review B* **102**, 100403 (2020), publisher: American Physical Society.
- [30] C. Dai and F. Ma, *Applied Physics Letters* **118**, 112405 (2021).
- [31] D. Hayashi, Y. Shiota, M. Ishibashi, R. Hisatomi, T. Moriyama, and T. Ono, *Applied Physics Express* **16**, 053004 (2023).
- [32] J. Sklenar and W. Zhang, *Physical Review Applied* **15**, 044008 (2021).
- [33] H. Chen, Y. Chen, T. Wang, Y. Xie, A. F. Franco, and J. Q. Xiao, *IEEE Transactions on Magnetics* **56**, 1 (2020).
- [34] M. Li, J. Lu, and W. He, *Physical Review B* **103**, 064429 (2021).
- [35] Also known as bilinear or quadratic interaction.
- [36] S. Lepadatu, H. Saarikoski, R. Beacham, M. J. Benitez, T. A. Moore, G. Burnell, S. Sugimoto, D. Yesudas, M. C. Wheeler, J. Miguel, S. S. Dhesi, D. McGrouther, S. McVitie, G. Tatara, and C. H. Marrows, *Scientific Reports* **7**, 1640 (2017).
- [37] X. Xie, X. Wang, W. Wang, X. Zhao, L. Bai, Y. Chen, Y. Tian, and S. Yan, *Advanced Materials* **35**, 2208275 (2023).
- [38] A. S. Jenkins, B. Lacoste, G. Geranton, D. Gusakova, B. Dieny, U. Ebels, and L. D. Buda-Prejbeanu, *Journal of Applied Physics* **115**, 083911 (2014).
- [39] A. F. Franco and P. Landeros, *Journal of Physics D: Applied Physics* **51**, 225003 (2018).
- [40] A. Sud, K. Yamamoto, K. Z. Suzuki, S. Mizukami, and H. Kurebayashi, *Physical Review B* **108**, 104407 (2023).
- [41] Y. Wang, Y. Zhang, C. Li, J. Wei, B. He, H. Xu, J. Xia, X. Luo, J. Li, J. Dong, W. He, Z. Yan, W. Yang, F. Ma, G. Chai, P. Yan, C. Wan, X. Han, and G. Yu, *Nature Communications* **15**, 2077 (2024), publisher: Nature Publishing Group.
- [42] M. M. Subedi, K. Deng, B. Flebus, and J. Sklenar, *Journal of Physics: Condensed Matter* **36**, 375802 (2024), publisher: IOP Publishing.
- [43] A. Vansteenkiste, J. Leliaert, M. Dvornik, M. Helsen, F. Garcia-Sanchez, and B. Van Waeyenberge, *AIP Advances* **4**, 107133 (2014).
- [44] Y. S. Gui, N. Mecking, X. Zhou, G. Williams, and C.-M. Hu, *Physical Review Letters* **98**, 107602 (2007).
- [45] A. A. Tulapurkar, Y. Suzuki, A. Fukushima, H. Kubota, H. Maehara, K. Tsunekawa, D. D. Djayaprawira, N. Watanabe, and S. Yuasa, *Nature* **438**, 339 (2005).
- [46] J. C. Sankey, P. M. Braganca, A. G. F. Garcia, I. N. Krivorotov, R. A. Buhrman, and D. C. Ralph, *Physical Review Letters* **96**, 227601 (2006).
- [47] L. Liu, T. Moriyama, D. C. Ralph, and R. A. Buhrman, *Physical Review Letters* **106**, 036601 (2011).
- [48] M. T. Hossain, S. Lendinez, L. Scheuer, E. T. Papaioannou, and M. B. Jungfleisch, *Applied Physics Letters* **119**, 212407 (2021).
- [49] M. Harder, Z. X. Cao, Y. S. Gui, X. L. Fan, and C.-M. Hu, *Physical Review B* **84**, 054423 (2011).
- [50] S. O. Demokritov, *Journal of Physics D: Applied Physics* **31**, 925 (1998).
- [51] J. Inoue, *Journal of Magnetism and Magnetic Materials* **136**, 233 (1994).
- [52] H. J. Waring, N. A. B. Johansson, I. J. Vera-Marun, and T. Thomson, *Physical Review Applied* **13**, 034035 (2020).
- [53] H. J. Mamin, D. Rugar, J. E. Stern, R. E. Fontana, and P. Kasiraj, *Applied Physics Letters* **55**, 318 (1989).
- [54] L. Exl, S. Bance, F. Reichel, T. Schrefl, H. Peter Stimming, and N. J. Mauser, *Journal of Applied Physics* **115**, 17D118 (2014).
- [55] S. O. Parreiras and M. D. Martins, *Physics Procedia 20th International Conference on Magnetism, ICM 2015*, **75**, 1142 (2015).
- [56] R. Weber, D.-S. Han, I. Boventer, S. Jaiswal, R. Lebrun, G. Jakob, and M. Kläui, *Journal of Physics D: Applied Physics* **52**, 325001 (2019).
- [57] A. Hrabec, F. J. T. Gonçalves, C. S. Spencer, E. Arenholz, A. T. N'Diaye, R. L. Stamps, and C. H. Marrows, *Physical Review B* **93**, 014432 (2016).
- [58] L D Landau and E. M. Lifshitz, *Quantum Mechanics - 3rd Edition*, Course of Theoretical Physics, Vol. Volume 3 (1977).